Angewandte Chemie International Edition

Angewandte International Edition Chemie

How to cite: *Angew. Chem. Int. Ed.* **2026**, e25646
doi.org/10.1002/anie.202525646

RESEARCH ARTICLE OPEN ACCESS

Alkyne-Based Dual-Function Self-Assembled Monolayers for Efficient and Stable p-i-n Perovskite Solar Cells

Ziyang Xia[1,2] | Haoxin Wang[1,3] | Seongmin Han[2] | Bin Cai[1] | Cheng Chen[1] | Yaosen Wang[1] | Shutong Duan[1] | Ming Cheng[1] | Sang Il Seok[2]

[1]Institute For Energy Research, Jiangsu University, Zhenjiang, China | [2]Department of Energy and Chemical Engineering, Ulsan National Institute of Science and Technology (UNIST), Ulsan, South Korea | [3]Macao Institute of Materials Science and Engineering (MIMSE), Macau University of Science and Technology, Taipa, Macao, China

Correspondence: Cheng Chen (chencheng@ujs.edu.cn) | Ming Cheng (mingcheng@ujs.edu.cn) | Sang Il Seok (seoksi@unist.ac.kr)

Received: 20 November 2025 | **Revised:** 25 March 2026 | **Accepted:** 9 April 2026

Keywords: donor–acceptor | perovskite solar cell | self-assembled monolayer | thermal stability | triple bonds

ABSTRACT

Recently, self-assembled monolayers (SAMs) have garnered significant attention in the field of perovskite solar cells (PSCs). Replacing flexible alkyl chains with conjugated linkers can significantly enhance the material's performance. Traditional conjugation modulation primarily relies on carbon–carbon double bonds (C═C), whereas the use of carbon–carbon triple bonds (C≡C) to expand the conjugated system of SAM materials has been rarely reported, and the influence of introducing triple bonds on material properties and device performance remains unclear. In this work, we design a novel donor–acceptor (D–A) structured SAM, named ABT, by incorporating a C≡C linker between the D–A moiety and the anchor group. The introduction of a C≡C bond effectively extends the conjugated system of the material, significantly enhancing its thermal stability and charge transport properties. As a result, ABT-based devices achieve a champion power conversion efficiency (PCE) of 26.19%, surpassing the reference BT-based devices (24.92%), along with exceptional thermal and long-term operational stability. This work provides a rational molecular design strategy for high-performance and stable D–A type SAMs, thereby facilitating the commercialization of PSCs.

1 | Introduction

Self-assembled monolayers (SAMs) have emerged as pivotal tools for interface engineering in perovskite solar cells (PSCs), driving power conversion efficiencies (PCEs) beyond 27% in recent years [1–5]. Structurally, SAMs consist of three key components: a head group, a linker unit, and an anchoring group, all of which directly influence interfacial charge transport and device stability [6, 7]. Therefore, the design and development of novel SAM materials with superior performance have become a primary research focus in the field of PSCs [8, 9]. Among these structural components, the linker unit plays a critical role: non-conjugated linkers weaken intermolecular interactions and disrupt charge transport [10, 11], while conventional conjugated motifs (e.g., benzene rings, alkenes, thiophenes) introduce trade-offs between device performance and stability [12–14]. For instance, benzene rings induce torsional strain, which breaks π-electron delocalization [15, 16], and alkenes are prone to cis–trans isomerization and thermal degradation, leading to charge recombination and limiting device lifetime [17–19]. Thus, targeted modulation of the linker unit to simultaneously optimize molecular conjugation, rigidity, and thermal stability remains an urgent challenge.

Ziyang Xia and Haoxin Wang contributed equally to this work.

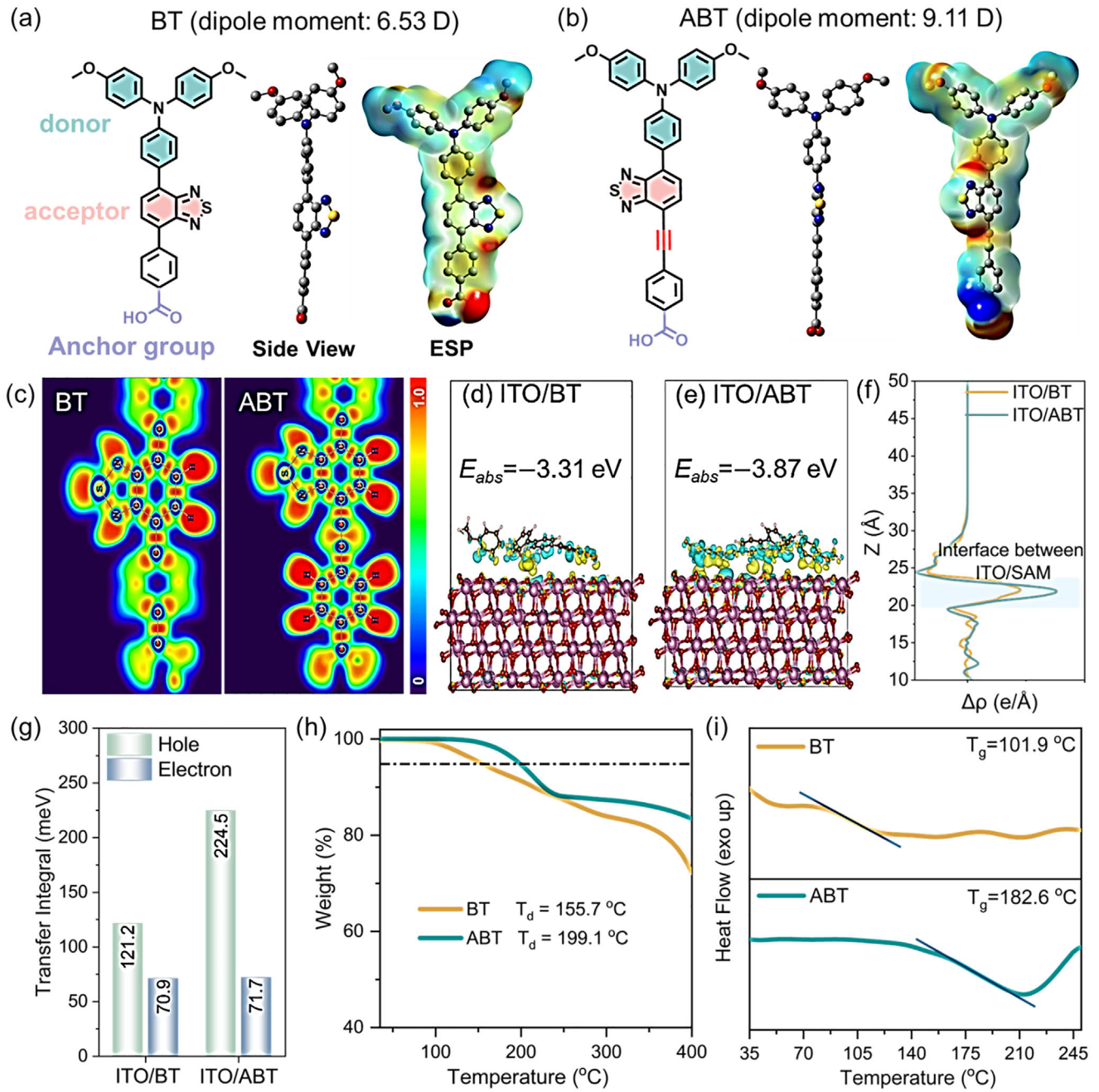

FIGURE 1 | Molecular structure, dipole moments, side view, and ESP maps of (a) BT and (b) ABT; (c) Comparison of the localized ELF between BT and ABT; Total charge–density difference plots for the adsorption structures of (d) ITO/BT and (e) ITO/ABT; (f) Calculated charge–density displacement profiles along the vertical direction to the ITO surface; (g) The calculated hole and electron transfer integrals on ITO/ABT and ITO/BT interface; (h) TGA and (i) DSC curves of BT and ABT.

Herein, we propose the carbon–carbon triple bond (alkynyl linker, –C≡C–) as a transformative linker unit. Its linear geometry and orthogonal π-bonds facilitate unbroken π-electron delocalization for efficient charge transport, while its high bond dissociation energy and structural rigidity help mitigate conformational distortion and thermal degradation [20, 21]. Capitalizing on these advantages, we rationally designed a novel donor–acceptor (D–A) structured SAM by strategically inserting a linear alkyne linker between the D–A core (triphenylamine–benzothiadiazole, TPA–BTD) and the benzoic acid anchoring group (Figure 1a). The resulting molecule, named ABT (Figure 1b), exhibits markedly improved electronic and structural characteristics. The introduction of alkyne linker enhances π-electron delocalization via its linear conjugated structure, facilitating vertical hole transport and thereby promoting charge collection efficiency. Furthermore, the alkyne linker serves as a rigid, linear π-conjugated linker that encourages a planar molecular conformation, thereby reducing molecular rotation and increasing bond energy, both of which contribute to enhanced molecular stability. Consequently, ABT-based PSCs achieve a champion PCE of 26.19%, outperforming the reference BT-based device (24.92%). Notably, the ABT-based devices demonstrate a twofold enhancement in stability under

both thermal stress and long-term operational conditions compared to the BT-based counterparts. This work provides a rational design strategy for developing high-performance and stable D-A SAMs, contributing to improved efficiency and durability of PSCs.

2 | Results and Discussion

Compared to the reference SAM BT, ABT is strategically designed by inserting an alkynyl linker between the D–A core TPA-BTD and the benzoic acid anchor group (Figure 1a,b). As illustrated in Scheme S1, the synthetic routes for SAMs BT and ABT are highly similar, differing primarily in the coupling strategy used to connect the D–A core TPA-BTD with the anchor group. SAM BT is synthesized via Suzuki coupling reaction, while ABT incorporates an alkyne linker through a Sonogashira reaction. The chemical structure of ABT was verified using nuclear magnetic resonance (NMR) spectroscopy and high-resolution mass spectrometry (HRMS), as depicted in Figures S1–S4.

The introduction of alkynyl linker enhances the molecular dipole moment, as demonstrated by the calculated dipole moments of BT and ABT, which are 6.53 and 9.11 D, respectively (Figures 1a,b, and S5). Moreover, the improved molecular coplanarity and rigidity lead to an increase in the binding energy from 31.73 kcal/mol for BT to 33.20 kcal/mol for ABT, along with a strengthened intermolecular interaction (Figure S6). As revealed by the molecular charge density distribution and electrostatic potential (ESP) analyses (Figures S7 and 1a,b), the alkynyl linker exhibits pronounced electron-withdrawing characteristics. This property synergizes with the benzoic acid anchor to facilitate electron delocalization throughout the molecular framework, as evidenced by frontier orbital analysis and electron localization function (ELF) calculations (Figure 1c). Notably, ABT demonstrates a red-shifted absorption edge relative to BT, with corresponding optical bandgaps of 2.21 and 2.30 eV, respectively (Figure S8 and Table S1). The narrowed bandgap originates from the combined electron-withdrawing effect and enhanced conjugation of the alkynyl linker, which collectively reduces the electron cloud density and thereby lowers the molecular energy levels [22].

To assess charge transfer efficiency at the SAM/ITO interface, we conducted DFT calculations on optimized SAM-ITO adsorption configurations. As depicted in Figure 1d,e, ABT exhibits slightly negative adsorption energies (E_{ads}) ranging from −3.31 eV (BT reference) to −3.87 eV, confirming stronger interfacial binding than BT. This is primarily attributed to the introduction of the triple bond, which effectively enhances the molecular dipole moment of SAM. Analysis of total charge density differences (Figures 1d,e and S9) and *Z*-axis charge displacement profiles (perpendicular to the ITO surface, Figure 1f) reveals enhanced electron cloud delocalization and more uniform distribution at the ABT/ITO interface, indicating improved vertical charge transport. Furthermore, calculated hole/electron transfer integrals at the ITO/SAM interface demonstrate that ABT exhibits a hole transfer integral twice that of BT, while electron transfer remains comparable (Figure 1g). Meanwhile, the hole mobility of ABT, measured at 8.36×10^{-5} $cm^2V^{-1}s^{-1}$ using the space-charge-limited technique on hole-only devices, is higher than that of BT, which is measured at 4.75×10^{-5} $cm^2V^{-1}s^{-1}$ (Figure S10). These results underscore ABT's superior hole transport capability into the ITO substrate.

Thermogravimetric analysis (TGA) and differential scanning calorimetry (DSC) were employed to characterize the thermal stability of the two molecules ABT and BT. As illustrated in Figure 1h,i, ABT demonstrates enhanced thermal stability, with both its decomposition temperature ($T_d = 199.1°C$, defined at 5% weight loss) and glass transition temperature ($T_g = 182.6°C$) being higher than those of BT ($T_d = 155.7°C$, $T_g = 101.9°C$). These results indicate that the rigid alkynyl linker, with its higher bond energy, effectively enhances molecular thermal stability, suggesting its potential for improving the thermal stability of PSCs.

The introduction of the triple bond and the improved dipole moment enable ABT to effectively modulate the work function (W_F) of the ITO electrode, thereby reducing the energy offset between the ITO W_F and the perovskite valence band maximum (VBM). As illustrated in Figure 2a,b, the measured W_F values for bare ITO, ITO/BT, and ITO/ABT are 4.68, 4.49, and 4.78 eV, respectively. The higher W_F of ITO/ABT corresponds to a reduced hole extraction barrier at the perovskite interface. Furthermore, the HOMO energy levels of ITO/BT and ITO/ABT are determined to be −5.06 and −5.26 eV, respectively. The 0.2 eV downward shift in the HOMO level of ITO/ABT, resulting from the moderate electron-withdrawing nature of the alkynyl linker, effectively minimizes interfacial energy losses within the device [23]. These results align well with DFT calculations (Figure S11) and cyclic voltammetry (CV) measurements (Figure S12).

X-ray photoelectron spectroscopy (XPS) analysis reveals significant upshifts of the In 3d and Sn 3d core levels for both BT and ABT samples toward higher binding energies (Figures 2c and S13a), conclusively demonstrating atomic-level SAM formation on the ITO substrate via strong chemical bonding with the oxide surface. Concurrently, the O 1s spectra exhibit four distinct peaks at 533.9, 533.2, 531.8, and 530.6 eV, attributable to H_2O, —OH, C—O, and In—O species, respectively [24, 25]. Notably, the C—O component accounts for 27.1% in ABT versus 26.2% in BT, indicating enhanced ABT retention on the ITO surface due to strengthened intermolecular interactions (Figure S13b). Similarly, cyclic voltammetry (CV) measurements at different scan rates corroborate the trend in the surface density of SAM molecules on ITO (Figure S14). Furthermore, conductive atomic force microscopy (C-AFM) measurements show that ITO/ABT exhibits a higher, more uniform average surface current than ITO/BT (Figures 2d and S15), providing direct evidence of superior charge-transport capability.

In inverted PSCs, the SAM can serve as a template influencing the perovskite crystallization [26]. As shown in Figure 2e, the contact angles of the perovskite precursor solution on ITO/BT and ITO/ABT are 7.0° and 7.4°, respectively, indicating similarly excellent wettability. Scanning electron microscope (SEM) images show that the perovskite films deposited on both BT- and ABT-modified ITO substrates exhibit comparable grain size and morphology (Figures 2f, S16, and S17). X-ray diffraction (XRD) patterns further confirm that the crystallinity of the perovskite remains largely consistent on both SAMs-modified substrates, as evidenced by the similar (001) crystal face diffraction peak intensity (Figures 2g and S18). This uniformity can be attributed

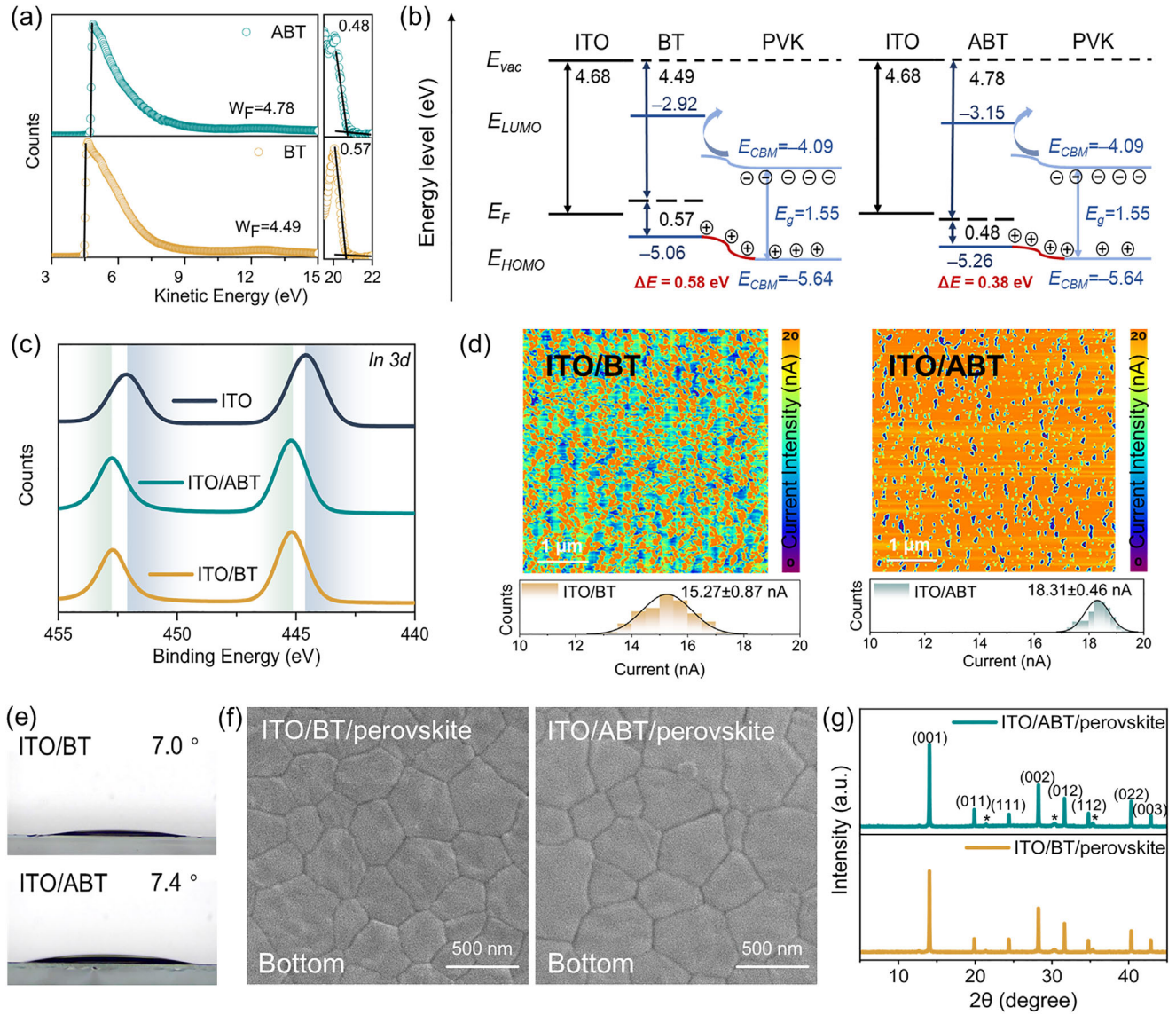

FIGURE 2 | (a) UPS spectra of SAMs-modified ITO; (b) Schematic diagram of energy level alignment; (c) XPS spectra of the In 3d core level for bare ITO and ITO covered with BT or ABT; (d) c-AFM images and corresponding surface potential distribution histogram of ITO substrates covered with BT and ABT; (e) Contact angles of perovskite precursor solution droplets on BT- and ABT-modified ITO substrates; (f) SEM images of the buried interface of perovskite films deposited on BT- and ABT-modified ITO substrates; (g) XRD patterns of perovskite films deposited on BT- and ABT-modified ITO substrates.

to the similar physicochemical environments provided by the two SAMs. Together, these findings indicate that the device performance is mainly determined by the charge transfer capability of the SAMs, rather than variations in the quality of the perovskite film.

Based on these findings, the photovoltaic performances of devices with the architecture ITO/SAM/perovskite/$PDAI_2$&3MTPAI/C_{60}/BCP/Ag (using BT and ABT as SAMs, a mixture of 1,4-phenylenediammonium diiodide ($PDAI_2$) and 3-(methylthio)propylamine hydroiodide (3MTPAI) as passivation layer, as illustrated in Figure 3a,b, respectively) were systematically evaluated. After optimizing the SAM deposition process (Figure S19), statistical analysis via box plots (Figure 3c) reveals that devices employing the alkynyl linker-modified SAM (ABT) achieve significantly enhanced PCE and reduced performance variability, particularly in open-circuit voltage (V_{OC}) and fill factor (*FF*). Figure 3d compares the *J*–*V* curves of champion devices for different PSCs, with detailed parameters summarized in Table 1. The ABT-based champion device achieved a PCE of 26.19%, with a V_{OC} of 1.184 V, a short-circuit current density (J_{SC}) of 25.87 mA cm^{-2}, and a *FF* of 85.49%, outperforming the BT-based device (PCE = 24.92%, V_{OC} = 1.170 V, J_{SC} = 25.51 mA cm^{-2}, *FF* = 83.49%) and widely recognized SAM Me-4PACz-based device (PCE = 25.31%, V_{OC} = 1.177 V, J_{SC} = 25.60 mA cm^{-2}, *FF* = 84.00%; Figure S20). Notably, ABT utilizing the alkynyl linker stands out as one of the best-performing D–A type SAMs (Table S2). Furthermore, stabilized power output (SPO) measurements recorded at the maximum power point (MPP) yielded stabilized PCE values of 26.08% and 24.91% for ABT- and BT-based devices, respectively (Figure S21). The J_{SC} values derived from *J*–*V* measurements align closely with

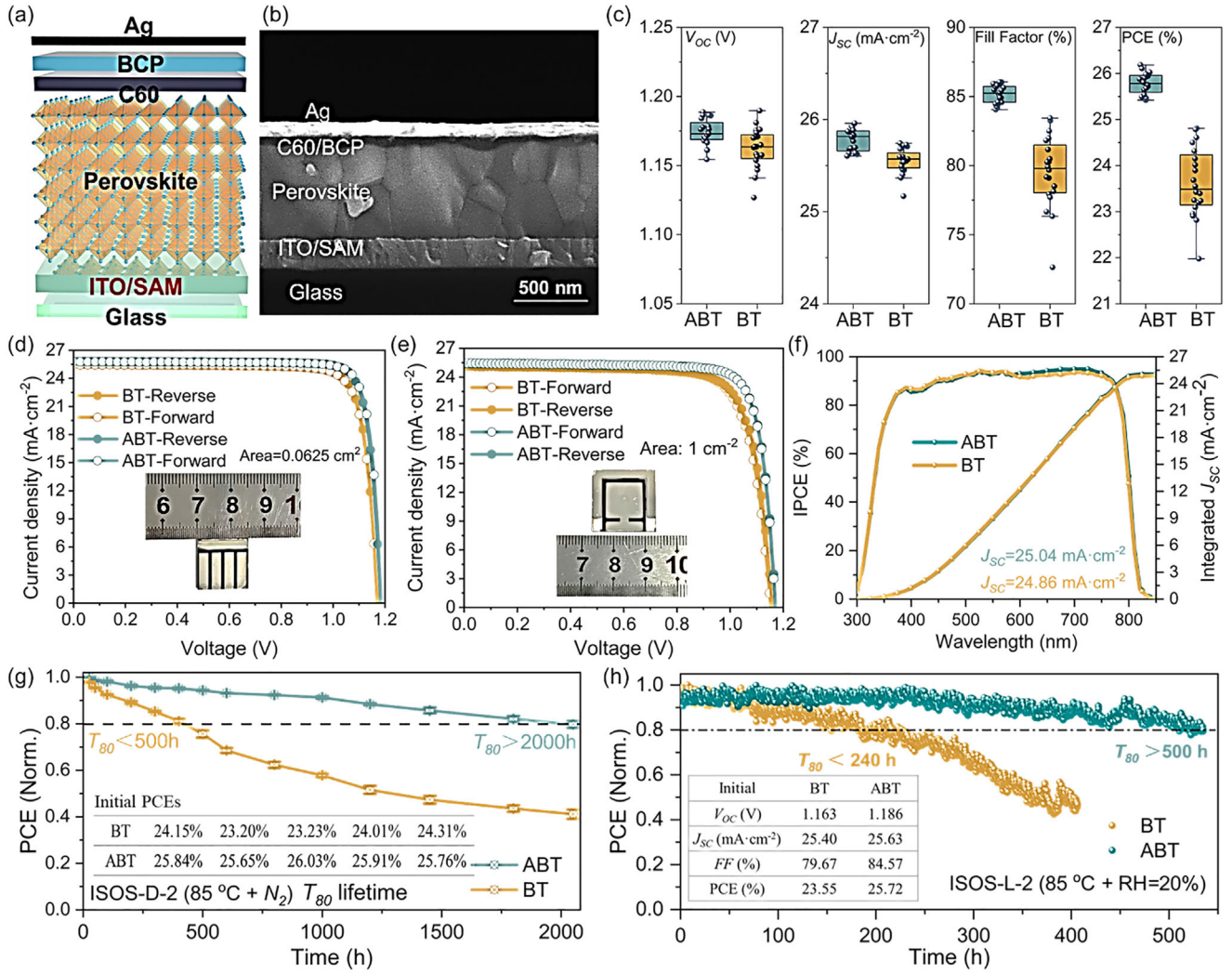

FIGURE 3 | (a) Device architecture and (b) cross-sectional SEM image of the fabricated p-i-n PSCs; (c) Statistical box plots of V_{OC}, J_{SC}, *FF* and PCE for BT and ABT based PSC devices (20 devices per group from the same batch); *J-V* curves of champion devices based on different SAMs with active area of (d) 0.0625 cm^2 and (e) 1.0 cm^2; (f) IPCE spectrum of the champion devices based on different SAMs; (g) Thermal stability of unencapsulated PSCs measured under ISOS-D-2 protocols; (h) Operational stability under maximum power point tracking under continuous illumination in N_2 atmosphere following ISOS-L-2 standards (initial efficiency of the test devices in the table).

TABLE 1 | Photovoltaic parameters of PSCs based on BT and ABT with an active area of 0.0625 cm^2.

SAM		Scan direction	V_{OC} (V)	J_{SC} (mA·cm^{-2})	*FF* (%)	*PCE* (%)
ABT	Champion PCE	Reverse	1.184	25.87	85.49	26.19
		Forward	1.185	25.74	85.54	26.09
	Average PCE	Reverse	1.173 ± 0.009	25.75 ± 0.13	85.30 ± 0.81	25.76 ± 0.29
BT	Champion PCE	Reverse	1.170	25.51	83.49	24.92
		Forward	1.171	25.45	83.24	24.81
	Average PCE	Reverse	1.163 ± 0.015	25.55 ± 0.14	79.54 ± 2.61	23.63 ± 0.75

the integrated J_{SC} obtained from the incident photon-to-electron conversion efficiency (IPCE) spectra (Figure 3f), confirming the reliability of the data. The IPCE spectra reveal a slight reduction in photo-response at short wavelengths (380–500 nm) for ABT-based devices, primarily due to the enhanced parasitic absorption induced by the incorporation of electron-deficient conjugated alkynyl linkers (Figures S22 and S23). Nonetheless, the loss is compensated by enhanced photo-response at long wavelengths (600–800 nm), which outweighs the parasitic absorption effect due to ABT's superior charge extraction and transfer capabilities [27]. To further assess the scalability of the device modified with SAMs, large-area devices with an active area of 1.0 cm^2 were

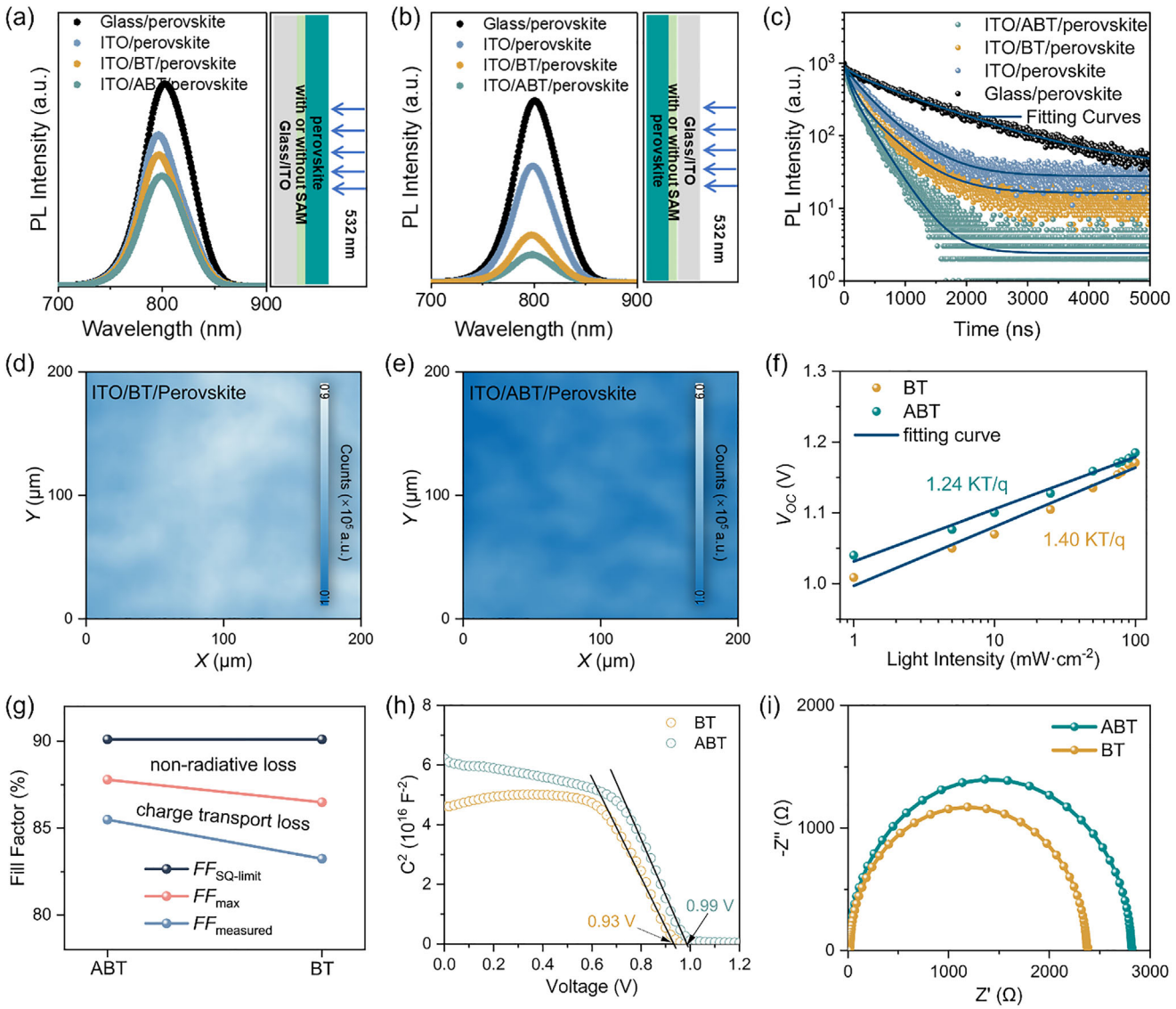

FIGURE 4 | (a) Steady-state PL spectra of perovskite films coated on SAMs substrates were extracted from (a) top surface and (b) bottom surface; (c) TRPL spectra (bottom surface), (d and e) 2D PL mapping images of perovskite film on different SAMs substrate. The incident light comes from the SAMs side; (f) Light-intensity dependence of V_{OC} for BT-based and ABT-based devices; (g) *FF* S-Q limits of devices with different SAMs; (h) Mott–Schottky curves and (i) EIS curves of full devices.

fabricated. The large-area ABT-based device achieved a PCE of 24.40% with a relative efficiency loss (REL) of 6.83%, significantly outperforming the BT-based counterpart, which exhibited a PCE of 22.68% and a higher REL of 8.99% (Figure 3e and Table S3).

The unencapsulated BT-based and ABT-based PSCs were aged at 85°C on a hotplate in a N_2-filled glovebox. After 2000 h, the ABT-based devices retained 80.6% of their initial PCE, significantly outperforming the BT-based devices, which retained only 41.2%, representing a 50% improvement in stability for the ABT-based PSCs (Figure 3g). This enhanced thermal stability can be attributed to the alkynyl linkers in ABT, which possess high bond energies that effectively mitigate thermally induced molecular conformational changes often associated with weak conjugation and low bond energies [28]. MPP tracking tests further confirmed the superior operational stability of ABT-based devices. The T_{80} lifetime (the time the device retains 80% of its initial performance) of ABT-based PSCs exceeded 500 h, compared to merely 240 h for BT-based devices (Figure 3h). The improved operational stability is attributed to the denser ABT assembly on ITO, thus suppressing interfacial ion diffusion between the perovskite and ITO [29, 30].

As previously established, the performance differentiation among PSCs primarily stems from the charge transfer capabilities of SAMs. To evaluate interfacial charge dynamics, we conducted steady-state photoluminescence (PL) and time-resolved photoluminescence (TRPL) measurements on perovskite films deposited on SAM-modified ITO substrates. The steady-state photoluminescence (PL) spectra (Figure 4a,b), acquired from different sides of the films, consistently show substantial quenching of the perovskite emission when deposited on ITO compared to quartz glass, unequivocally indicating efficient hole transfer from the perovskite to the ITO substrate. Notably, SAM-modified ITO exhibits enhanced PL quenching efficiency in the order

ITO/ABT > ITO/BT, signifying more efficient hole extraction and suppressed non-radiative charge recombination through electron transfer to the ITO Fermi level [31–33]. The conclusions were further validated by TRPL analysis. As shown in Figure 4c and Table S4, the mean PL lifetime decreases systematically: ITO/ABT/perovskite (427.59 ns) < ITO/BT/perovskite (283.85 ns) < ITO/perovskite (206.95 ns). The shortest lifetime for the ABT interface directly correlates with accelerated hole extraction and minimized non-radiative recombination. Complementary 2D PL mapping (Figure 4d,e) corroborates this trend, revealing lower perovskite PL intensity for ABT, which confirms enhanced interfacial hole extraction and reduced non-radiative losses in ABT-based devices. The light-intensity-dependent V_{OC} analysis (Figure 4f) demonstrates that ABT-based devices exhibit a lower ideality factor (1.24 KT/q) compared to BT-based counterparts (1.41 KT/q). This correlates with reduced *FF* loss attributable to non-radiative recombination (Figure 4g). Investigation of interfacial electrical characteristics reveals that ABT-based devices possess a higher built-in potential (V_{bi} = 0.99 V) than BT-based devices (V_{bi} = 0.93 V, Figure 4h), indicating an enhanced driving force for photogenerated charge carrier separation. Electrochemical impedance spectroscopy (EIS, Figure 4i and Table S5) further confirms this advantage. ABT-based devices show lower series resistance (R_s) and higher recombination resistance (R_{rec}), which are key metrics for improved charge injections and suppressed recombination at the perovskite/ABT interface [34]. Dark current measurements (Figure S24) provide additional validation of these interfacial charge dynamics. Collectively, these results elucidate that the incorporation of alkyne-linked SAMs with extended electron delocalization not only promotes efficient hole extraction but also simultaneously suppresses vertical electron diffusion, achieving optimized interfacial charge management.

3 | Conclusion

In summary, we have developed a molecular design strategy that incorporates alkyne linkers between the D–A moiety and the anchor group in D–A type SAMs. This approach effectively enhances π-electron delocalization and restrains conformational flexibility commonly observed in conventional counterparts. The alkyne linkers not only promote electronic delocalization and facilitate hole collection at the interface but also serve as rigid linkers that suppress thermally induced conformational disorder, thereby enhancing thermal stability. As a result, devices based on the novel ABT SAM achieved a champion PCE of 26.19%, outperforming the reference BT-based devices (24.92%), along with significantly improved stability under both thermal stress and long-term operation. This work provides a rational design strategy for high-performance and stable D–A type SAMs, contributing to the simultaneous advancement of efficiency and operational stability in PSCs.

Acknowledgements

This work was financially supported by the financial support from the National Natural Science Foundation of China (Grants 22279046, 22179053), Natural Science Excellent Youth Foundation of Jiangsu Provincial (BK20220112), Special Foundation for Carbon Peak Carbon Neutralization Technology Innovation Program of Jiangsu Province (BE2022026-2), China Scholarship Council program (202508320283). Z.X., S.H., and S.I.S. acknowledge financial support from the Basic Science Research Leader Program (RS-2018-NR030954) and the Nano & Material Technology Development Program (RS-2024-00449449) through the National Research Foundation of Korea (NRF), funded by the Ministry of Science, ICT & Future Planning (MSIP). The authors extend their gratitude to Mr. Shijun Qiu (from Scientific Compass www.shiyanjia.com) for providing invaluable assistance with the UPS analysis, Mr. Guowei Liao and Ms. Zhangli Pei (from SCI-GO www.sci-go.com) for the NMR and HRMS analysis.

Conflicts of Interest

The authors declare no conflicts of interest.

Data Availability Statement

The data that support the findings of this study are available from the corresponding author upon reasonable request.

References

1. W. Jiang, G. Qu, X. Huang, et al., "Toughened Self-assembled Monolayers for Durable Perovskite Solar Cells," *Nature* 646 (2025): 95–101, https://doi.org/10.1038/s41586-025-09509-7.

2. National Renewable Energy Laboratory (NREL), Best Research Cell Effciencies, https://www.nrel.gov/pv/assets/pdfs/best-researchcell-efficiencies. (accessed November 2025).

3. X. Wang, J. Li, R. Guo, et al., "Regulating Phase Homogeneity by Self-assembled Molecules for Enhanced Efficiency and Stability of Inverted Perovskite Solar Cells," *Nature Photonics* 18 (2024): 1269–1275, https://doi.org/10.1038/s41566-024-01531-x.

4. B. Dong, M. Wei, Y. Li, et al., "Self-assembled Bilayer for Perovskite Solar Cells With Improved Tolerance Against Thermal Stresses," *Nature Energy* 10 (2025): 342–353, https://doi.org/10.1038/s41560-024-01689-2.

5. X. He, H. Chen, J. Yang, et al., "Enhancing Hole Transport Uniformity for Efficient Inverted Perovskite Solar Cells Through Optimizing Buried Interface Contacts and Suppressing Interface Recombination," *Angewandte Chemie International Edition* 63 (2024): e202412601, https://doi.org/10.1002/anie.202412601.

6. A. Magomedov, A. Al-Ashouri, E. Kasparavičius, et al., "Self-Assembled Hole Transporting Monolayer for Highly Efficient Perovskite Solar Cells," *Advanced Energy Materials* 8 (2018): 1801892, https://doi.org/10.1002/aenm.201801892.

7. P. Mao, W. Bi, J. Lv, Z. Zhang, B. Wang, and Y. Zhong, "Decoding Buried Interfaces in Perovskite Solar Cells: Core Issues, Strategic Engineering, and Prospects for High-Efficiency Stable Devices," *Advanced Science* 12 (2025): e12523.

8. K. Guo, H. Tang, L. Han, et al., "Self-Assembled Monolayer: Revolutionizing p-i-n Perovskite Solar Cells," *ACS Energy Letters* 10 (2025): 4882–4910, https://doi.org/10.1021/acsenergylett.5c02024.

9. X. Yu, X. Sun, Z. Zhu, and Z. Li, "Stabilization Strategies of Buried Interface for Efficient SAM-Based Inverted Perovskite Solar Cells," *Angewandte Chemie International Edition* 64 (2025): e202419608, https://doi.org/10.1002/anie.202419608.

10. J. Yang, G. Qu, Y. Qiao, et al., "Flexibility Meets Rigidity: A Self-assembled Monolayer Materials Strategy for Perovskite Solar Cells," *Nature Communications* 16 (2025): 6968, https://doi.org/10.1038/s41467-025-62388-4.

11. B. Zhou, M. Li, Q. Xiong, et al., "Soft Conjugation Extension Strategy of Self-assembled Molecules for Achieving Efficient and Mechanically Stable Flexible Perovskite Solar Cells," *Energy & Environmental Science* 18 (2025): 8803–8814, https://doi.org/10.1039/D5EE03823E.

12. G. Qu, S. Cai, Y. Qiao, et al., "Conjugated Linker-boosted Self-assembled Monolayer Molecule for Inverted Perovskite Solar Cells," *Joule* 8 (2024): 2123–2134, https://doi.org/10.1016/j.joule.2024.05.005.

13. T. Wu, M. Zhang, X. Gao, et al., "Self-Assembled Monolayers for Perovskite Solar Cells: Molecular Design and Chemical Synthesis," *ACS Nano* 19 (2025): 24508–24535, https://doi.org/10.1021/acsnano.5c05601.

14. S. Yuan, C. Ge, T. Zhang, et al., "Conjugated Bisphosphonic Acid Self-Assembled Monolayers for Efficient and Stable Inverted Perovskite Solar Cells," *Journal of the American Chemical Society* 147 (2025): 24662–24671, https://doi.org/10.1021/jacs.5c05801.

15. W. R. Hollingsworth, J. Lee, L. Fang, and A. L. Ayzner, "Exciton Relaxation in Highly Rigid Conjugated Polymers: Correlating Radiative Dynamics With Structural Heterogeneity and Wavefunction Delocalization," *ACS Energy Letters* 2 (2017): 2096–2102, https://doi.org/10.1021/acsenergylett.7b00535.

16. D. Khan, X. Liu, G. Qu, A. R. Nath, P. Xie, and Z.-X. Xu, "Nexuses Between the Chemical Design and Performance of Small Molecule Dopant-Free Hole Transporting Materials in Perovskite Solar Cells," *Small* 19 (2023): 2205926, https://doi.org/10.1002/smll.202205926.

17. M. K. J. ter Wiel, R. A. van Delden, A. Meetsma, and B. L. Feringa, "Light-Driven Molecular Motors: Stepwise Thermal Helix Inversion During Unidirectional Rotation of Sterically Overcrowded Biphenanthrylidenes," *Journal of the American Chemical Society* 127 (2005): 14208–14222, https://doi.org/10.1021/ja052201e.

18. J. Saha, S. Banerjee, S. Malo, A. K. Das, and I. Das, "Thermally Activated Geometrical Regioselective E→ Z Isomerization-Enabled Cascade Sequences of Conjugated Dienals: Experimental and DFT Studies," *Chemistry–A European Journal* 29 (2023): e202302335, https://doi.org/10.1002/chem.202302335.

19. Y. Zheng, T. Niu, L. Chao, Y. Xia, and Y. Chen, "Stability of Hole-selective Self-assembled Monolayers in Inverted Perovskite Solar Cells," *Journal Energy Chemistry* 107 (2025): 74–86, https://doi.org/10.1016/j.jechem.2025.03.032.

20. Y. Wang, Q. Liao, G. Wang, et al., "Alkynyl-Functionalized Head-to-Head Linkage Containing Bithiophene as a Weak Donor Unit for High-Performance Polymer Semiconductors," *Chemistry of Materials* 29 (2017): 4109–4121, https://doi.org/10.1021/acs.chemmater.7b01052.

21. F. Yang, H. Fang, E. Guo, et al., "Oligomerized Electron Acceptors With Alkynyl Linkages to Suppress Electron-Phonon Coupling for Low-Energy-Loss Organic Solar Cells," *Angewandte Chemie, International Edition* 64 (2025): e202501302, https://doi.org/10.1002/anie.202501302.

22. C. Cui, X. Fan, M. Zhang, J. Zhang, J. Min, and Y. Li, "A D–A Copolymer of Dithienosilole and a New Acceptor Unit of Naphtho[2,3-c]Thiophene-4,9-dione for Efficient Polymer Solar Cells," *Chemical Communications* 47 (2011): 11345, https://doi.org/10.1039/c1cc14132e.

23. G. Qu, L. Zhang, Y. Qiao, et al., "Self-assembled Materials With an Ordered Hydrophilic Bilayer for High Performance Inverted Perovskite Solar Cells," *Nature Communications* 16 (2025): 86, https://doi.org/10.1038/s41467-024-55523-0.

24. Y. Zhou, X. Huang, J. Zhang, et al., "Interfacial Modification of NiO X for Highly Efficient and Stable Inverted Perovskite Solar Cells," *Advanced Energy Materials* 14 (2024): 2400616, https://doi.org/10.1002/aenm.202400616.

25. Y. Feng, Y. Wang, H. Yang, et al., "Homogenized Self-Assembled Molecules for Inverted Perovskite Solar Cells," *Angewandte Chemie, International Edition* 64 (2025): e202505876, https://doi.org/10.1002/anie.202505876.

26. Q. Cao, T. Wang, X. Pu, et al., "Co-Self-Assembled Monolayers Modified NiO X for Stable Inverted Perovskite Solar Cells," *Advanced Materials* 36 (2024): 2311970, https://doi.org/10.1002/adma.202311970.

27. Z. Xia, X. Feng, T. Wu, et al., "Dimeric Carbazole Core Based Dopant-Free Hole Transport Material for n-i-p Planar Perovskite Solar Cell," *Advanced Functional Materials* 34 (2024): 2408423, https://doi.org/10.1002/adfm.202408423.

28. C. Lv, Y. Miao, J. Wang, et al., "Enhanced Efficiency and Stability of Inverted Perovskite Solar Cells via Isomerization Engineering of Self-Assembled Monolayers," *Angewandte Chemie International Edition* 64 (2025): e202513338, https://doi.org/10.1002/anie.202513338.

29. J. Song, H. Liu, W. Pu, et al., "Thermal Instability Originating From the Interface Between Organic–inorganic Hybrid Perovskites and Oxide Electron Transport Layers," *Energy & Environmental Science* 15 (2022): 4836–4849, https://doi.org/10.1039/D2EE02649J.

30. Y. Feng, Y. Wang, H. Yang, et al., "Homogenized Self-Assembled Molecules for Inverted Perovskite Solar Cells," *Angewandte Chemie International Edition* 64 (2025): e202505876, https://doi.org/10.1002/anie.202505876.

31. X. Zhang, B. Li, S. Zhang, et al., "A Spiro-type Self-assembled Hole Transporting Monolayer for Highly Efficient and Stable Inverted Perovskite Solar Cells and Modules," *Energy & Environmental Science* 18 (2025): 468–477, https://doi.org/10.1039/D4EE01960A.

32. Y. Zhang, Z. Yang, M. Li, et al., "Indenocarbazole-Engineered Self-Assembled Monolayers With Sterically Tuned π-Stacking for High-Efficiency p–i–n Perovskite Solar Cells," *Advanced Energy Materials* 15 (2025): 2501855, https://doi.org/10.1002/aenm.202501855.

33. H. Chen, Q. Cao, X. Pu, et al., "Strong Coupling of NiOx and Self-Assembled Molecules via Inserted Reductant for High-Performance Inverted Perovskite Solar Cells," *Advanced Materials* 37 (2025): e10553, https://doi.org/10.1002/adma.202510553.

34. X. Xu, S. Li, C. Shan, et al., "Adhesively Bridging Co-Self-Assembled Monolayer and Perovskite via In Situ Polymerization for Enhanced Stability of Inverted Perovskite Solar Cells," *Advanced Materials* 37 (2025): 2505745, https://doi.org/10.1002/adma.202505745.

Supporting Information

Additional supporting information can be found online in the Supporting Information section.

The experimental details are provided in the Supporting Information.

Supporting File: anie72248-sup-0001-SuppMat.docx.